*Analytica Chimica Acta*, 283 (1993) 98–119
Elsevier Science Publishers B.V., Amsterdam

# Synchrotron radiation-induced x-ray microanalysis

K. Janssens, L. Vincze and F. Adams

*Department of Chemistry, University of Antwerp (UIA), Universiteitsplein 1, B-2610 Wilrijk / Antwerp (Belgium)*

K.W. Jones

*Department of Applied Science, Brookhaven National Laboratory, Upton, Long Island, NY 11973 (USA)*

(Received 12th October 1992)

**Abstract**

The qualities and limitations of synchrotron radiation-induced x-ray microfluorescence (SRXRF) spectrometry are discussed in comparison with those of more conventional microchemical techniques such as secondary ion microscopy and electron probe microanalysis. Examples of the analysis of particulates and the two-dimensional mapping of elemental species are given. Two new developments in connection with SRXRF are discussed: the use of microscopic x-ray absorption spectrometry and the predicted performance of SRXRF spectrometers installed with third-generation synchrotron sources.

*Keywords:* X-ray fluorescence spectrometry; Synchrotron radiation

Synchrotron radiation-induced x-ray microfluorescence (SRXRF) spectrometry is the microscopic analogue of the well established multi-elemental bulk analysis method of (energy-dispersive) x-ray fluorescence (EDXRF) spectrometry. In the latter method, radiation from bremsstrahlung tubes or radioactive sources is employed to induce emission of element-specific radiation by sample atoms; usually sample areas of 1–2 $cm^2$ are irradiated to yield (in the case of EDXRF) detectable count rates in the range $10^3$–$10^4$ counts $s^{-1}$. To achieve the same count rate when an area of only, e.g., 100 $\mu m^2$ ($10^{-6}$ $cm^2$) is employed, x-ray sources that are typically $10^6$ times more intense are required. Such extremely intense x-ray fluxes are provided by electron storage rings where radiation is produced by forcing a beam of light elementary particles (electrons, positrons) in a quasi-circular orbit. At the location where the relativistic particle beam is forced to alter its direction by means of suitable magnetic fields, an intense beam of polarized, polychromatic radiation is produced in a cone oriented tangentially to the particle beam path. The vertical opening angle of the cone (typically a few mrad) is related to the energy of the circulating particles which is in the range 0.1–10 GeV. The maximum intensity is emitted in the plane of the storage ring itself. This radiation is linearly polarized in the plane; slightly above and below the storage ring plane, the radiation is elliptically polarised.

Typical energy distributions of the x-rays produced at bending magnets are shown in Fig. 1. In addition to bending magnets, other magnetic structures called wigglers and undulators are employed to produce even higher x-ray fluxes. These devices operate by forcing the particle beam into multiple oscillatory trajectories and are installed in the straight sections of the storage rings.

*Correspondence to:* K. Janssens, Department of Chemistry, University of Antwerp (UIA), Universiteitsplein 1, B-2610 Wilrijk/Antwerp (Belgium).

0003-2670/93/$06.00 © 1993 – Elsevier Science Publishers B.V. All rights reserved

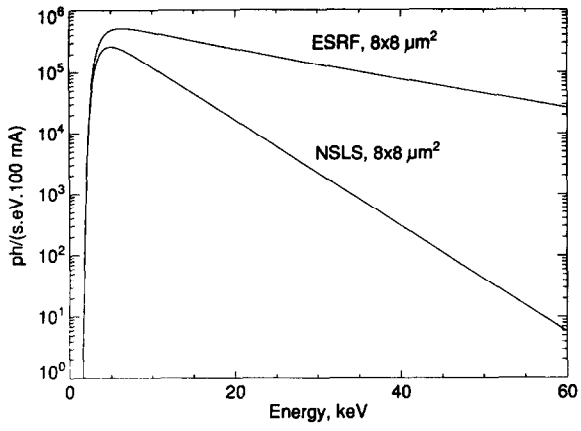


Fig. 1. Photon flux available at (0.8-T) ESRF and NSLS bending magnet beam lines using a $8 \times 8$ $\mu m^2$ pin hole collimator at 30 and 10 m, respectively, from the tangent point.

In the last 5 years, as a result of the increasing availability of electron storage rings as sources of highly intense, collimated and polarized x-rays in the energy range between 1 and 30–40 keV, a number of x-ray fluorescence microprobes have been constructed. An overview of some of the characteristics of these instruments is presented in Table 1.

The analytical properties of the various instruments are mainly determined by two factors: the characteristics of the storage ring/x-ray source at which they are installed and the way in which radiation originating from the ring is transformed into a microbeam. At Hasylab (Hamburg, Germany) [1] and the NSLS (Brookhaven National Laboratories, Upton, NY) [2], white light microprobes are in operation; at these stations, collimated pencil beams are used to perform sensitive trace element mapping with minimum detection limits (MDLs) in the 1–10 ppm range and with a lateral resolution of the order of 10 $\mu$m. At SRS (Daresbury, UK) [3], SSRL (Stanford, Ca) [4] and the Photon Factory (Tsukuba) [5], focused monochromatic microbeams are employed. Some of the optical configurations listed in Table 1 have only very recently been tested in practice and the analytical qualities of the corresponding SRXRF spectrometers still need to be evaluated [6,7].

In their most recent biannual review of x-ray spectrometry, Török and Van Grieken [8] considered the availability of intense small-sized beams for use in XRF experiments as one of the major developments in x-ray spectrometry, in addition to the use of laser-plasma sources, ultra-trace analysis by total reflection XRF (TXRF) and structural analysis by means of extended x-ray absorption fine structure (EXAFS) [9].

Most microanalytical methods such as secondary ion mass spectrometry (SIMS), proton-induced x-ray emission ($\mu$-PIXE) and electron probe x-ray microanalysis (EPXMA) combine a number of useful qualities with one or more undesirable properties. This also applies to SRXRF. However, SRXRF also represents a unique combination of advantageous properties that are not found elsewhere. Similarly to SIMS, SRXRF is capable of trace level microanalysis but does not have any of the disadvantages asso-

TABLE 1

Characteristics of currently operating X-ray microprobes

| Storage ring | $E_c$ (keV) [a] | Optical system | Energy (keV) | Spot size ($\mu m^2$) |
|---|---|---|---|---|
| DCI | 1.9 | Curved graphite crystal | 8–20 | – |
| | | Bragg–Fresnel lens | 10 | $2 \times 2$ |
| Hasylab | 31.7 | Pin hole | White | $3 \times 3$ |
| | | Conical capillary | White | ? |
| NSLS | 5 | Pin hole | White | $5 \times 5$, or larger |
| Photon Factory | 1.9 | Wolter | 10 | $3 \times 10$ |
| SSRL | 2.0 | KirkPatrick–Baez | 10–20 | $3 \times 3$ |
| VEPP-3 | 5.4 | Channel-cut monochromator | 10–60 | – |

[a] $E_c$ = critical energy of electron storage ring.

ciated with a destructive mass spectrometric technique. In addition to the damage that is inflicted by an ion beam on a sample surface, another significant disadvantage of SIMS is that the collected secondary ion intensities are very difficult to quantify; the use of elaborate empirical calibration procedures is required in order to do so. This calibration problem arises mainly as a result of the very complicated processes that give rise to the formation of the secondary ions. In contrast, the interaction of x-ray photons with matter is relatively simple, very well known and analytically describable. The combination of the capability to perform sensitive elemental mapping with the proven accuracy and reliability of quantitative XRF makes SRXRF a very interesting analytical technique.

Some of the weak and strong points of SRXRF can be understood when SRXRF is considered in comparison with its closest analogues, $\mu$-PIXE and EPXMA. Essentially, these three methods differ only in the type of energy carriers that are being used in the micro beam. In all instances, the energetic particle is used to eject a core-level electron from a target atom, while the intensity and energy of the resulting characteristic radiation are measured with an Si(Li) detector. The overall efficiency of photon-induced x-ray emission (i.e., the number of characteristic photons produced per primary photon) is $10^2$–$10^3$ times higher than in the case of electron- or proton-induced emission, and this quantity increases with increasing atomic number [10]. Accordingly, SRXRF is more suitable than EPXMA or $\mu$-PIXE for trace determinations of the heavier elements (atomic number $Z > 20$–$25$). Also, per characteristic photon produced, the energy deposited in the sample using SRXRF is a factor of $10^2$–$10^3$ lower than in EPXMA; the difference is even larger with $\mu$-PIXE [11,12].

In addition to the production efficiency for characteristic radiation, the MDLs achievable with an x-ray-based technique are also determined by the importance of the continuous background in the collected EDXRF spectra. In this respect, another important difference between the interaction of photons and charged particles with matter is the probability of scattering interactions. As a result of many (in)elastic collisions, the retardation of energetic charged particles in solids gives rise to a bremsstrahlung continuum. In the case of x-ray fluorescence, each primary photon either does not undergo any scattering interaction at all or (in the worst case) encounters one or two (in)elastic collisions with sample atoms before it is either absorbed (photoionization) or escapes from the solid. Accordingly, nearly background-free XRF spectra can be obtained when monochromatic photon excitation is employed, yielding (sub-)ppm level detection limits for selected elements (see Fig. 4). Only in the region at or just below the primary energy do (in)coherent scatter peaks contribute significantly to the background.

Owing to the linear polarization of the synchrotron radiation in the storage ring plane, a further decrease in the scatter background level can be realised if the detector is also positioned in this plane and at 90° to the incident beam. As shown in Fig. 4, this effect makes it possible to achieve ppm MDL values with SRXRF employing polychromatic excitation [2].

An additional advantage of an x-ray microprobe (XRM) is that it can be operated in air or in an inert gas atmosphere such as helium; also, samples need not be conducting. A weak point of an XRM is its limited lateral resolution (see Table 1). This property is directly related to the currently attainable beam sizes but is also influenced by other factors (see next section).

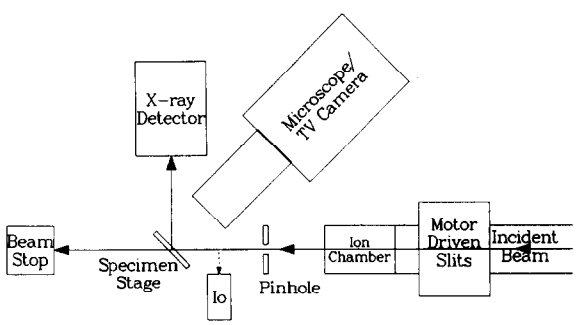


Fig. 2. Schematic diagram of the NSLS XRM. The pin hole–sample and sample–detector distances are of the order of a few cm.

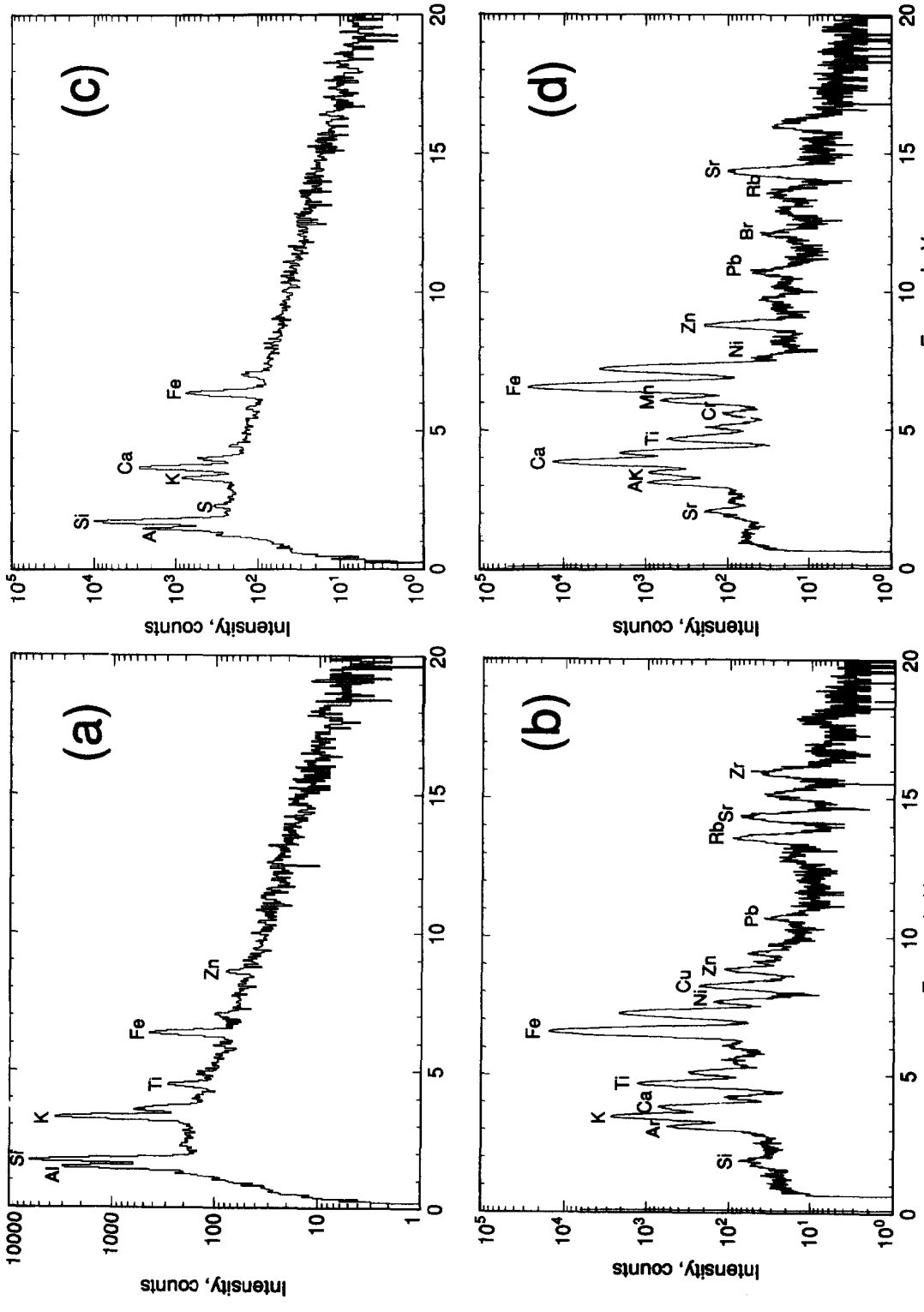


Fig. 3. X-ray spectra of two environmental particles of diameter 10–15 μm. (a, c) Electron-induced x-ray spectra; (b, d) synchrotron radiation-induced x-ray spectra.

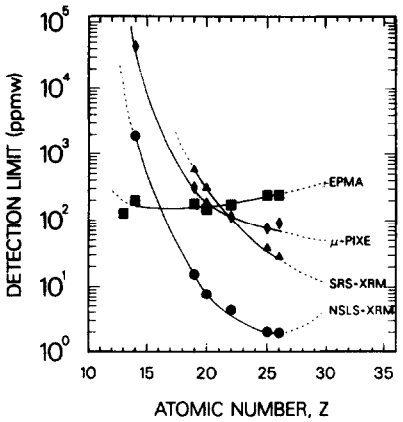


Fig. 4. MDL values derived from x-ray spectra of K309 glass microspheres of 20–30 μm diameter generated using different instruments and techniques. Adapted from [13].

In what follows, first the capabilities and limitations of currently operating SRXRF instruments are outlined by means of a few examples. The applicability of SRXRF to individual particle analysis is briefly discussed and a comparison of SRXRF with SIMS and EPXMA illustrates some of the (dis)advantages of SRXRF as a multi-elemental mapping technique. Next, the use of x-ray absorption near edge structure (μ-XANES) as a technique combinable with μ-SRXRF in the same experimental set-up and which yields chemical information on selected elemental species is mentioned. Finally, the predicted performance and applications of future SRXRF spectrometers, to be installed with third-generation synchrotron rings such as the European Synchrotron Radiation Facility (ESRF, Grenoble) or the APS (Advanced Photon Source, Argonne, IL), are discussed.

## EXPERIMENTAL

For the x-ray microprobe experiments, the instrument at the X26A beamline of the NSLS (National Synchrotron Light Source) was employed. After emerging from the storage ring ultra-high vacuum (UHV), the beam is defined by four tantalum slits and further collimated by a $5 \times 5$ or $8 \times 8$ $\mu m^2$ crossed slit system. The sample is positioned at 45° to the incoming beam. A schematic diagram of the instrument is shown in Fig. 2.

As shown in Fig. 1, the low-energy part of the polychromatic energy spectrum impinging on the sample is heavily absorbed by the beryllium end windows of the beam pipe and the air path between the collimator slits and the sample. The specimen is viewed by a horizontally mounted stereozoom binocular microscope, equipped with a TV camera. For the analysis of particulates, an $8 \times 8$ $\mu m^2$ collimator was employed to define the beam size. X-ray spectra were collected by locating a particle on the filter using the microscope, moving it into the beam and maximizing the detectable count rate. For the elemental mapping experiments, a specific $100 \times 100$ $\mu m^2$ area of a grain of Carnmenellis Granite was studied. In this area, elemental maps were collected, first by EPXMA (using a 25-kV electron beam), then by SRXRF and finally by SIMS (employing a 30-kV $O^-$ beam). During the SRXRF experiment, a collimator yielding a $5 \times 5$ $\mu m^2$ photon beam was employed. The collection of the $512 \times 512$ pixel SIMS maps took about 2 h of instrument time, including the alignment of the ion-optical system. The collection of the potassium and sodium x-ray maps ($140 \times 200$ pixels) using EPXMA took about 1 h. The synchrotron radiation-induced x-ray images were collected using a dwell time of 50 s per pixel; x-ray images $25 \times 35$ pixels in size were collected taking a total instrument time of about 12 h to acquire. The XANES spectra were also collected at the NSLS XRM and took ca. 1 h each to acquire, using a 1-s collection time at each energy. The spectra in Fig. 7a and b were collected using an energy increment of 0.6 eV and those in Fig. 7c with a 0.3-eV step size.

## SRXRF AT CURRENT SYNCHROTRON FACILITIES

In general, microchemical techniques may be employed for two generic types of studies: the analysis of minute samples such as microscopic particles and fibres, and the visualization of the distribution of elemental species in or on the surface of samples of larger dimensions with

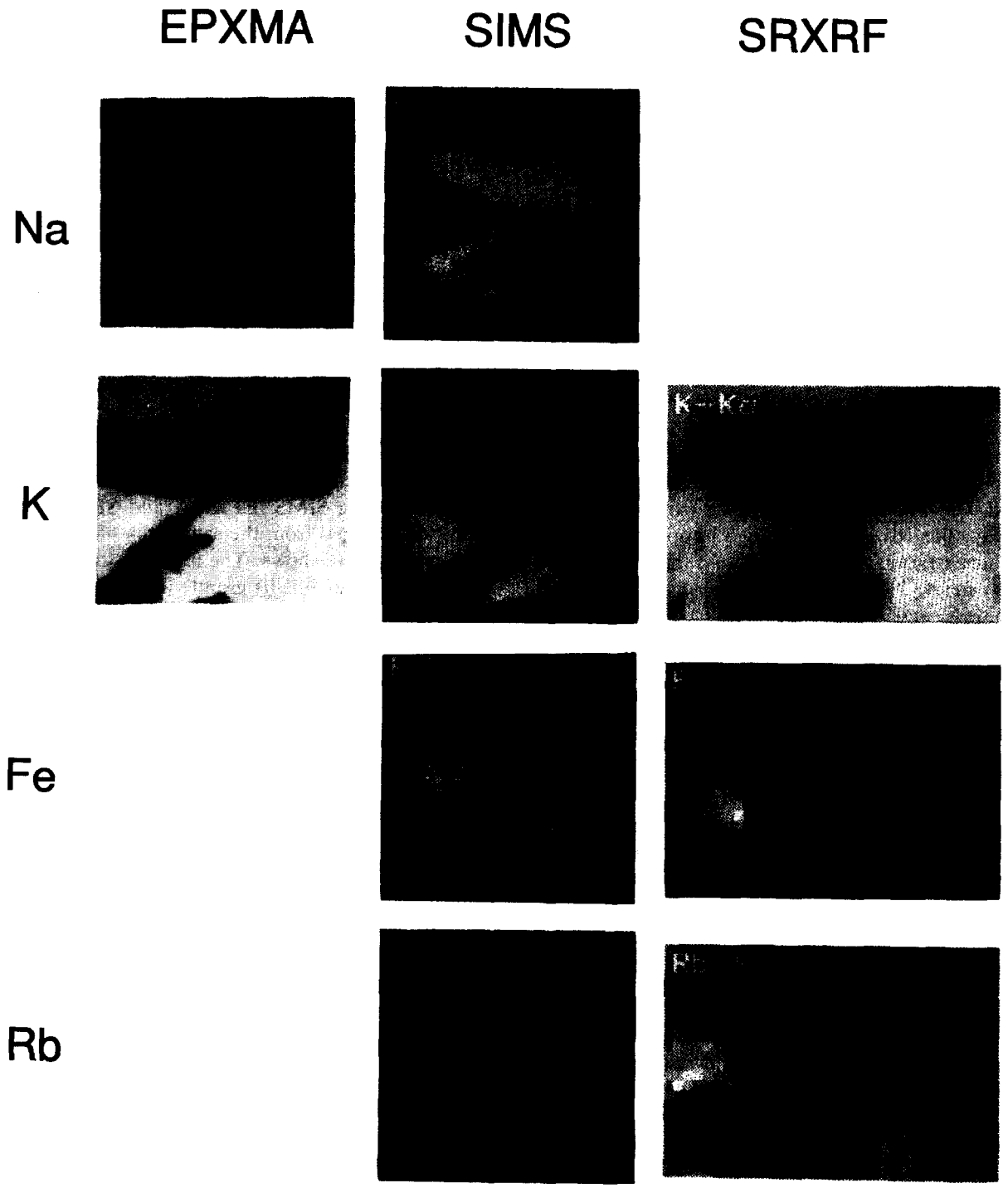


Fig. 5. Elemental maps of various major and trace constituents in selected area of a grain of microperthitic granite. Left column, EPXMA images; middle column, SIMS images; right column, SRXRF images. The dimensions of the lamellae shown in most of the maps are ca. $30 \times 100$ $\mu m^2$. Adapted from [17].

μm-size lateral resolution. In this section, examples of both types of analysis are discussed.

*Particulate analysis*

In Fig. 3, the applicability of SRXRF for the characterization of individual microscopic particles is illustrated. Individual particle analysis of aerosols by means of an automated electron microprobe analyser has proved to be a convenient technique for revealing the composition and relative importance of air pollution sources. In Fig. 3a–d, synchrotron radiation (SR) and electron-induced x-ray spectra of individual environmental particles having a mean diameter of ca. 10–15 μm are presented. Whereas in the EPXMA spectra (Fig. 3a and c), only the major constituents of the aluminosilicate particles are visible, in the x-ray-induced spectra (Fig. 3b and d) peaks corresponding to trace and minor constituents such as Ni, Cu, Pb, Br, Rb, Sr and Zr can be observed (e.g., the Rb signal in Fig. 3d corresponds to a concentration of ca. 50 ppm). As the NSLS XRM is operated in an air atmosphere, the low energetic Si and Al K$\alpha$ lines are heavily absorbed in the air path between the sample and detector.

In Fig. 4, the MDLs achievable at this instrument for the analysis of National Institute of Science and Technology (NIST) K309 Glass Microspheres of diameter 20–30 μm are compared with those obtained at the SRS XRM (see Table 1) and with those derived from electron- and proton-induced x-ray spectra of the same material (see [13] for details). In contrast to the NSLS XRM, at SRS a 15-keV monochromatic beam of primary radiation is employed. In the case of EPXMA, a more or less uniform sensitivity in the 100 ppm range is obtained; for the other techniques, the MDL values vary considerable with atomic number. Corresponding to the maximum near 8 keV in the excitation spectrum available at the NSLS XRM (Fig. 1), the lowest MDL values are obtained for elements such as Mn and Fe. The optimum MDL of 2 ppm for Fe corresponds for a 26-μm diameter particle to an absolute detectable amount of ca. 3 fg of Fe. With the SRS microprobe, an MDL of Fe of ca. 30 ppm is obtained.

The MDL values plotted in Fig. 4 are valid for a 300-s counting time and for fairly large particles (diameter 20–30 μm), compared with the average size distribution of environmental aerosol particles (0.1–10 μm). For particle diameters smaller than 10 μm, a much diminished x-ray yield is observed while the background intensity increases as a significant portion of the primary photons interact with the substrate rather than with the particles themselves. Accordingly, higher MDL values than those plotted in Fig. 4 are obtained and a smaller difference in sensitivity between SRXRF and EPXMA is observed. Nevertheless, for the smallest particles analysable using current SRXRM instrumentation (ca. 7 μm in diameter), the NSLS XRM is still 5–10 times more sensitive than EPXMA for Ca and Pb [13].

*Elemental mapping*

In Fig. 5, elemental maps of various elements obtained using SIMS, EPXMA and SRXRF (at the NSLS XRM) from the same area of a geological material are shown. The material studied was a grain of Carnmenellis granite [14], consisting of a potassium-rich feldspar groundmass in which ex-solution lamellae of albite (a sodium-rich feldspar mineral) are found. The dark rectangular area in most of the images in Fig. 5 corresponds to such a lamella (approximate dimensions $30 \times 100$ $\mu m^2$).

In addition to a difference in major composition (Na/K) between the two phases, the average abundance of trace elements such as Fe, Rb and Sr in the two phases is also different. Most minor and trace elements are predominantly present in the K-rich phase; Goossens et al. [14] reported, e.g., $Rb_2O$ concentrations of 840 and 3 ppm in the K- and Na-rich feldspar phases, respectively.

The elemental maps shown in Fig. 5 illustrate several of the strong and weak points of SRXRF. First, in contrast to EPXMA, by means of which only the distribution of the major elements could be mapped (Fig. 5, left column), the NSLS XRM allows the study of the distribution of trace elements such as Fe and Rb, similarly as in SIMS (Fig. 5, right and middle columns). The most striking difference between SRXRF and the other two methods obviously is the lateral resolution of the various images. Whereas in EPXMA and

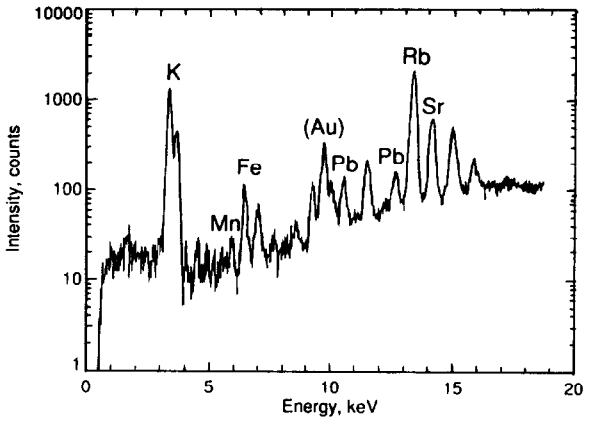


Fig. 6. SRXRF spectrum collected from a location in the K-rich phase of the granite samples shown in Fig. 5.

SIMS particle beams with submicrometre cross-sections are employed, for the SRXRF experiments a $5 \times 5$ $\mu m^2$ beam was used. In this way, the area of interest could be scanned in a reasonable amount of time (ca. 12 h) while a 50-s dwell time allowed for the collection of an EDXRF spectrum of sufficient statistics at each pixel.

Figure 6 shows one of these spectra, corresponding to a location in the K-rich phase. Owing to the limited spatial resolution, many of the finer details of the elemental distributions (such as the interconnection between the two lamellae) that are visible in both the SIMS and EPXMA images are lost in the SRXRF images.

Another factor affecting the lateral resolution is the difference in penetration depth between the three microbeam methods. Whereas using SIMS only the top 10–100 nm of the materials is being sampled (depending on the sputter time and beam intensity), 25-kV electrons will penetrate ca. 3–5 $\mu$m into the material, causing characteristic x-rays to emerge from a pear-shaped interaction volume of comparable size. For high-energy photons of, e.g., 10 and 20 keV, the $1/e$ penetration depth is ca. 130 and 950 $\mu$m, respectively, in the K-feldspar phase. Although the K K$\alpha$ radiation only escapes from the uppermost 10 $\mu$m, the more energetic Rb K$\alpha$ photons still have a comparable escape probability when originating from 300 $\mu$m deep. Accordingly, instead of only visualizing the two-phase structure on the upper surface of the grain (as in the SIMS maps in Fig. 5), the high-energy SRXRF images yield information on the distribution of elements deeper in the material. The highly penetrative character of photons can be used advantageously, e.g., for non-destructive structural investigations using computed microtomographic (CMT) techniques [15] or in the analysis of submerged structures such as fluid inclusions in minerals (see, e.g., [16]). On the other hand, as discussed in [17], it can also cause significant problems regarding the quantification of elemental maps as shown in the right-hand column of Fig. 5.

## NEW DEVELOPMENTS IN SRXRF

Currently, two new developments related to SRXRF merit attention. By employing more brilliant and more energetic x-ray sources, some of the limitations of current SRXRF instruments outlined in the previous section can be eliminated. Another development is the combination of the elemental speciation capabilities of SRXRF with the possibilities of x-ray absorption spectrometry ($\mu$-XAS) to yield chemical information on selected elemental species.

### *Microscopic x-ray absorption spectrometry*

In constrast to the relatively limited number of XRMs available worldwide (see Table 1), one of the major application areas of SR is absorption spectrometry. This technique is based on the irradiation of a sample with a highly monochromatic ($\Delta E/E \approx 10^{-4}$) x-ray beam of tunable energy. By scanning the energy over an absorption edge of an element of interest, called the central atom (e.g., Fe, when the Fe K-edge is scanned) in fractional eV steps and recording either the absorption of the beam in the sample (absorption XAS) or the intensity of the fluorescent radiation that is produced (fluorescence XAS), the fine structure on the absorption edge can be recorded. Two regions of x-ray absorption, the near edge (XANES) and the extended region (EXAFS), provide different structural information. The processing and interpretation of these features is not a trivial task, although efforts at standardization

are being made [18,19]. From EXAFS, information on the number, the atomic number and the distance of the neighbours of the central atoms may be derived. In the XANES region, data on the oxidation and coordination state of the central atom can be extracted from the position of the major edge and from the pre-edge features.

Both variants of absorption spectrometry have predominantly been used for bulk investigations of high-technology and catalyst materials (see, e.g., [20]). Iida and co-workers [21,22] reported $\mu$-XAS measurements using fluorescent detection with a lateral resolution of 20 $\mu$m in an instrument very similar to a monochromatic XRM. Iida [23] also demonstrated differences in the XANES spectra of Cr in the chromite, olivine and pyroxene phases of a peridotite rock sample. Using the microscopic arrangement of Fig. 2, but with the use of a Pt-coated 8:1 ellipsoidal mirror and a double-channel monochromator to focus and monochromate, respectively, the primary beam, Sutton et al. [24] also studied Cr in rocks using $\mu$-XANES and inferred the oxidation state of this element in 200-$\mu$m sized individual grains of lunar olivine and pyroxene from lunar basalt 15555. A beam of 180 × 205 $\mu$m was employed to obtain sufficient sensitivity for the detection of Cr at the 100 ppm level.

As an illustration of the applicability of $\mu$-XANES to the investigation of industrially important materials, in Fig. 7, Ti K-edge XANES spectra are shown which were collected using the same instrumentation as in [24]. In Fig. 7a, the XANES spectra of Ti metal and $Ti^{4+}$ in NIST 1832 standard glass demonstrate the shift to higher energies that the Ti K absorption edge undergoes with increasing oxidation state. The origin of the energy scale in Fig. 7 was arbitrarily fixed at the top of the sharp pre-edge peak visible in the $Ti^{4+}$ spectrum of Fig. 7a. This peak can be attributed to the $1s \rightarrow 3d$ transition; transitions of this type are forbidden by selection rules but can occur as a result of orbital mixing. Between the two profiles shown in Fig. 7a, a shift in half-height of about 13 eV can be observed, corresponding to ca. 3.25 eV per charge unit. Similar results were obtained by Waychunas [25]. Sutton et al. [24] observed a shift of 17 eV between Cr

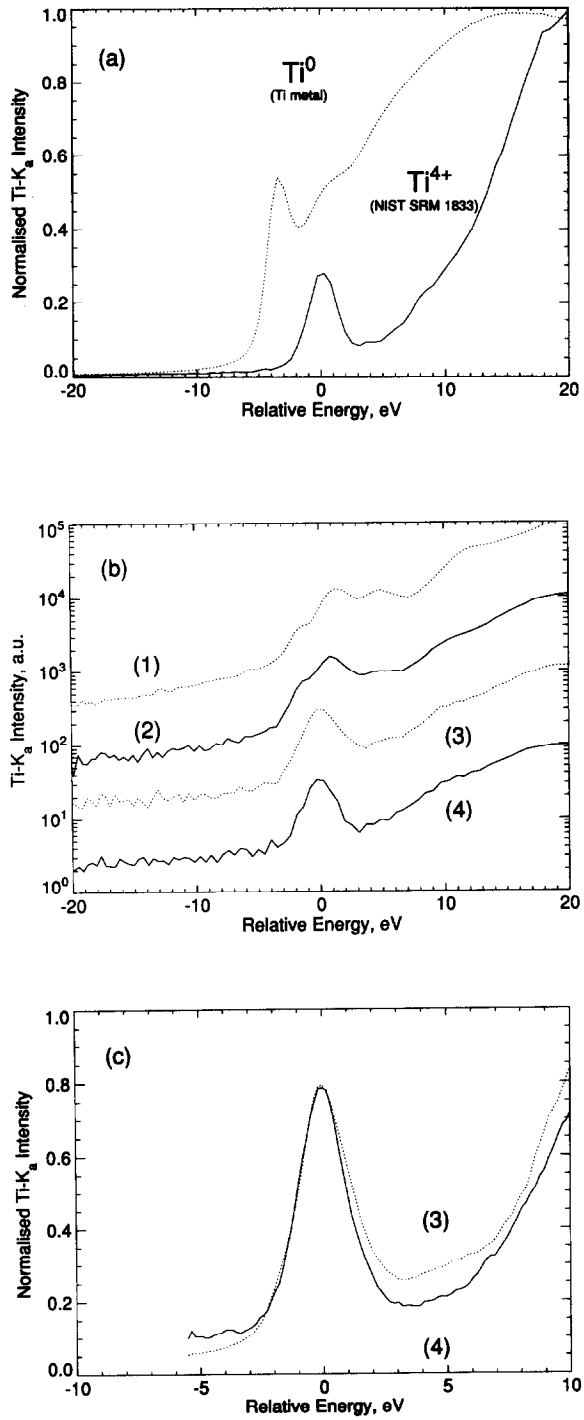


Fig. 7. (a) XANES spectra of the Ti K-edge for $Ti^0$ (Ti metal) and $Ti^{4+}$ ($TiO_2$ in NIST 1832 glass); (b) the same for $Ti^{4+}$ in various materials (see text); (c) high-resolution scan of the pre-edge peaks on curves 3 and 4 in (b).

metal ($Cr^0$) and $K_2CrO_4$ ($Cr^{6+}$) and arrived at approximately the same number.

As pointed out by various workers [21,24,25], a linear relationship between the edge position and the oxidation state of the central atoms can be readily established. In this way, by performing rapid energy scans over an absorption edge at various locations of the microbeam on the sample, chemical state mapping can be performed.

In addition to information on the chemical state of an element, data on the coordination of the central atom can also be extracted from the XANES region. In Fig. 7b, Ti K XANES spectra of $Ti^{4+}$ in various materials are shown. Curves 1 and 2 are very similar and correspond to anatase ($TiO_2$) and the so-called "Grace" silica, a co-gel of $SiO_2$ and $TiO_2$, respectively. Curves 3 and 4 were obtained from materials prepared from the co-gel through crystallization and which feature a zeolite structure (medium-pore zeolite ZSM-5) [26]. Curve 4 corresponds to titanium silicalite-1 (TS-1), a material which is an efficient catalyst for oxidation of organic compounds with hydrogen peroxide. The material from which curve 3 was obtained has the same structure as TS-1 but does not show the above-mentioned catalytic activity. Comparison of curves 1 and 2 indicates that the coordination of Ti in the co-gel is not very different from that in anatase. The typical three-peak pre-edge feature which can be observed in curves 1 and 2 has also been found by other workers [25,26] and is indicative of a regular octahedral site of Ti.

On the basis of Ti K XANES spectra of various Ti minerals, Behrens et al. [26] observed that with increasing distortion of the octahedral site, the central peak gains intensity and moves to slightly lower energies, as is the case in profiles 3 and 4. The width of the pre-edge peak in curve 3, which is broader than those obtained from compounds with uniform coordination (see the lower curve in Fig. 7a) indicates a co-existence of several environments for Ti in the inactive zeolite structure. Behrens et al. [26] suggested a 10:15:75 mixture of tetrahedral, square-pyramidal and octahedral coordinations. The shapes of the pre-edge peaks in curves 3 and 4 were recorded a second time with 0.3-eV resolution and are compared in Fig. 7c. Together with the deconvolution results presented in [26], the smaller width of the peak in curve 4 may indicate that in the catalytically active product, more Ti atoms are coordinated in a non-octahedral way. Further work, employing for instance data extracted from the EXAFS region of the Ti edge, needs to be done to confirm this hypothesis.

*Third-generation synchrotron sources*

A number of the limitations of SRXRF discussed in the previous section can be eliminated by using more intense photon sources. At currently operating storage rings, this can be done by using undulator or wiggler radiation instead of x-rays originating from a bending magnet. Rivers et al. [27] discussed SRXRF experiments at the 5-T superconducting wiggler of NSLS beamline X17B1. In addition to the advantage conferred by the higher intensity of the source, they pointed out that as a result of the higher divergence of the wiggler beam in the vertical plane, a poorer degree of polarization of the x-ray micro-beam is obtained than at the X26A bending magnet beamline [28].

An alternative is to employ bending magnet radiation from one of the third-generation synchrotron rings now currently under construction in Japan (SPRing-8 in Harima), the USA (APS at Argonne National Laboratories, IL) and in Europe (ESRF at Grenoble). For the last facility, the construction phase of which is virtually completed [29], the expected improvement in flux density and achievable MDLs when a collimated x-ray microprobe is installed at a 0.8-T bending magnet beamline was estimated. The predictions are based on a detailed Monte Carlo simulation of the interaction of a polarized, polychromatic photon beam with sample atoms [30,31]. The details of these calculations, which also include a comparison of the performance of optical devices for generating high-energy x-ray microbeams other than pin holes, are presented elsewhere [32]. Only the alternatives employing polychromatic forms of excitation will be discussed here.

Owing to the higher operating energy of the ESRF ring (6 GeV compared with 2.5 GeV for the NSLS), as shown in Fig. 1, the white syn-

chrotron spectrum obtained from an ESRF bending magnet is far more energetic than that obtained from an NSLS port. Whereas SRXRF trace elemental analysis at an NSLS bending magnet beamline is in practice restricted to the energy interval 3–30 keV (K lines of S to Cs) [33], using an ESRF x-ray source of similar type will allow for the excitation of the K lines of much heavier species such as the rare earth series or the platinum group elements. Although these elements can currently be determined using L-line radiation, detection limits for L lines are higher than those for K lines because the L fluorescence yields are smaller [33]. As a result of peak overlap, employing L lines for quantitative determinations is also more error prone and difficult than when K lines are used.

In Fig. 8, the predicted XRF spectrum which would be obtained if the white ESRF spectrum shown in Fig. 1 were used to excite an 80 mg $cm^{-2}$ sample of NIST SRM 1571 Orchard Leaves is compared with the corresponding experimental spectrum collected using the NSLS XRM. The simulated spectra in Fig. 8 were calculated assuming a degree of polarization of the primary radiation of 96%. (The discrepancies in the intensities of the K, Ti and Mn peaks between the simulated and experimental spectra for the NSLS case are attributed to microheterogeneity of the

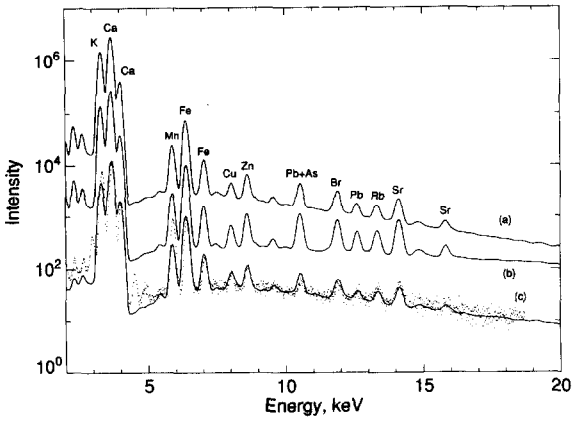


Fig. 8. Simulated (lines) and experimental (dots) SRXRF spectra derived from an 80 mg $cm^{-2}$ sample of NIST 1572 Orchard Leaves under different excitation conditions: (a) ESRF, capillary (see text); (b) ESRF, pin hole; (c) NSLS, pin hole.

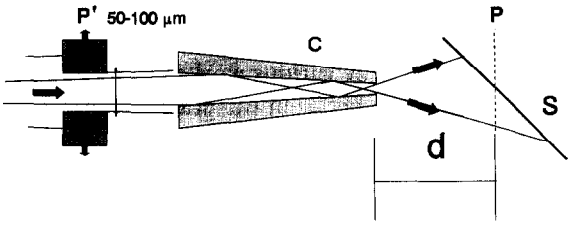


Fig. 9. Principle of capillary optics. $d$ = Distance between the far end of the capillary and the sample being irradiated; C = capillary; P = projection plane for the distributions of Fig. 11; S = sample at an angle of 45°; P′ = pin hole.

sample material [31].) Overall, in the low-energy region of the spectra (7–10 keV), for the ESRF case, in increase in the x-ray yield by a factor of 10 is observed compared with the NSLS case. As can be expected from the plots in Fig. 1, at higher energies a higher sensitivity increase is obtained while improved peak-to-background (P/B) ratios are also observed for, e.g., the Br, Sr and Rb peaks. These two phenomena cause the MDL values for this type of sample, which for the NSLS XRM are at the 2–3 ppm level for elements heavier than Fe, to decrease to the 0.3–1 ppm range [32].

In Fig. 8, the EDXRF spectrum that would be obtained if, instead of a simple pin hole arrangement, a conical glass capillary were to be used to define the ESRF x-ray beam is also shown. The operating principle of this type of device is shown in Fig. 9. X-ray photons of energy $E$ originating from the storage ring enter the capillary and are reflected on the inner walls of the glass tube, provided that they impinge on the walls at an angle smaller than the critical angle of total reflection $\theta_c$ $(E)$. Whereas parallel capillaries are used as x-ray wave guides (e.g., in microfluorescence and microdiffraction instruments employing conventional x-ray tubes [34]), tapered capillaries of the type shown in Fig. 9 can act as polychromatic focusing devices with high-energy filtering properties.

Engström et al. [6] demonstrated the use of these devices for focusing of SR beams. In view of their simplicity compared with e.g., ellipsoidal or toroidal mirrors, and the fact that they may be used to focus radiation for $\mu$-XAS experiments,

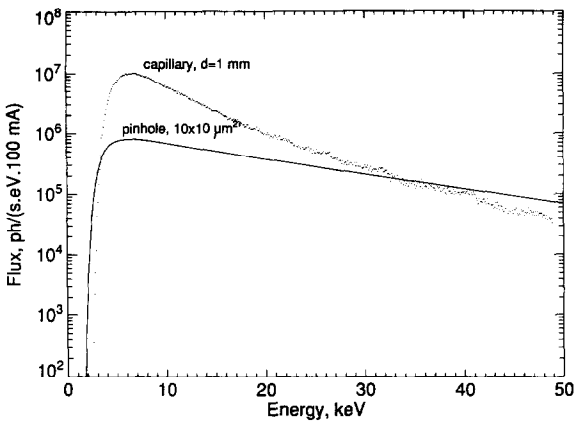


Fig. 10. X-ray flux available at an ESRF 0.8-T bending magnet transmitted by a $10 \times 10$ $\mu m^2$ pin hole (line) and by a glass capillary yielding the same spot at 1 mm from the capillary end (dots). See text.

these capillaries are currently considered to be very promising optical elements for hard x-ray focusing. For one of the devices tested in [6] (a capillary of 25 cm length, with i.d.. 58 and 1 $\mu$m at the beginning and end, respectively), Fig. 10 illustrates the energy-dependent focusing properties and the effect on the white ESRF spectrum. These results were obtained by means of a ray tracing code developed in this laboratory.

In Fig. 11, the predicted dimensions of the microbeam emerging from the capillary tip at different distances $d$ (see Fig. 9) are shown. Because the x-rays emerge from the tapered glass tube at an angle $\theta \leqslant \theta_c$ $(E)$ (which in general is larger than the divergence of the incoming SR beam), in order to maintain the small beam cross-sections defined by the end diameter of the capillary, the sample material to be investigated must be placed extremely close to the capillary end. As can be seen from Fig. 11, the beam cross-section rapidly increases with larger values of $d$. For the above-mentioned capillary and for a distance $d$ equal to 1 mm, a microspot of 100 $\mu m^2$ is obtained. In Fig. 10 the unfocused flux passing through a pin hole of the same area is also plotted. The gain in flux by a factor of 10–20 at the lower excitation energies results is a comparable sensitivity gain for elements in the $Z$ range from 19 (K) to 26 (Fe), as shown in Fig. 8. As a result of the diminishing focusing capabilities of the capillary with increasing energy, for heavier elements such as Rb and Sr, less favourable P/B ratios are obtained than in the pin hole case (Fig. 8, curve b).

*Conclusions*

Some of the strong and weak points of SRXRF as implemented at currently operating XRM facilities have been highlighted. It can be concluded that SRXRF is a valuable method for the determination of trace, minor and major elements and this it can profitably be used in parallel with electron and ion beam methods. Exciting

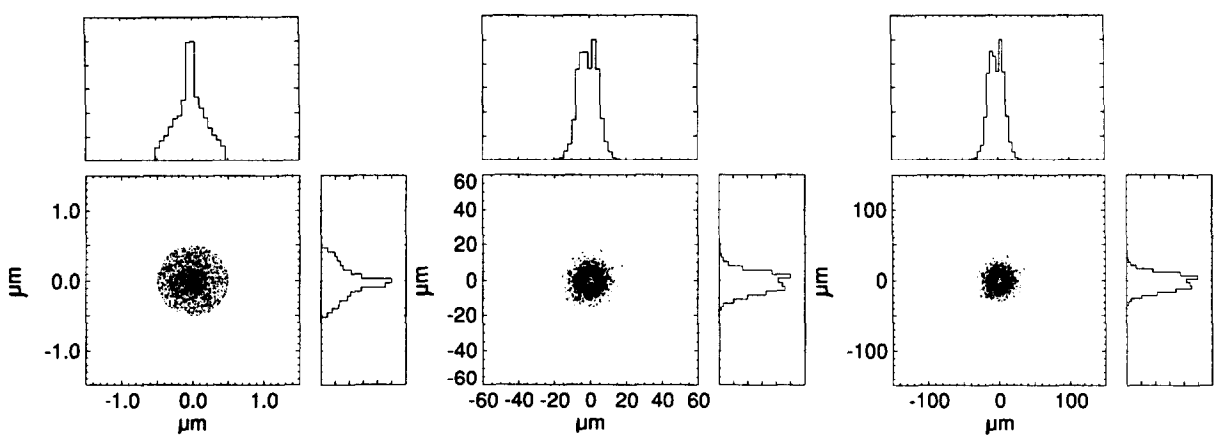


Fig. 11. Variation of the cross-section of the beam emerging from the capillary as a function of the distance $d$. Left 0 mm; middle 5 mm; right, 10 mm. Spot sizes of 1, 25 and 50 $\mu$m, respectively are achieved.

new horizons are opening up for SRXRF as third-generation X-ray sources become available, providing highly energetic and polarized photon beams of unprecedented intensity. In addition to the improvement in lateral resolution and in sensitivity that these new x-ray sources will induce, the enhancement of the elemental mapping capacity of SRXRF with the chemical speciation possibilities of $\mu$-XAS will significantly improve the scope and breath of x-ray microprobe analysis.

This work was supported by the Belgian National Science Fund NFWO and in part by the US Dept. of Energy under Contract DE-ACO2-76CH00016.

REFERENCES

1 M. Bavdas, A. Knöchel, P. Ketelsen, W. Petersen, N. Gurker, M.H. Salehi and T. Dietrich, Nucl. Instrum. Methods, A266 (1988) 308.
2 K.W. Jones, and B.M. Gordon, Anal. Chem., 61 (1989) 341A.
3 F. Van Langevelde, D.K. Bowen, G.H.J. Tros, R.D. Vis, A. Huizing and D.K.G. de Boer, Nucl. Instrum. Methods, A292 (1990) 719.
4 A.C. Thompson, J.H. Underwood, Y. Wu, R.D. Giaque, K.W. Jones and M.L. Rivers, Nucl. Instrum. Methods, A266 (1988) 318.
5 Y. Goshi, S. Aoki, A. Iida, S. Hayakawa, H. Yamaji and K. Sakurai, Jpn. J. Appl. Phys., 26 (1987) L1260.
6 P. Engström, S. Larsson, A. Rindby, A. Buttkewitz, S. Garbe, G. Gaul, A. Knöchel and F. Lechtenberg, Nucl. Instrum. Methods, A302 (1991) 547.
7 D. Erko and P. Chevallier, in A. Michette, G. Morreson and C. Buckley (Eds.), X-Ray Microscopy III, Springer, Berlin, New York, 1992, pp. 105–107.
8 S.T. Török and R.E. Van Grieken, Anal. Chem., 64 (1992) 180R.
9 J.W. Gilfrich, X-Ray Spectrom., 19 (1990) 45.
10 L.S. Birks et al., Appl. Phys., 35 (1964) 2578.
11 A.P. Mazzolini, G.J.F. Legge and C.K. Palaghy, Nucl. Instrum. Methods, 191 (1981) 217.
12 R.D. Vis, Scanning Microsc., 2 (1988) 977.
13 K. Janssens, F. Van Langevelde, F.C. Adams, R.D. Vis, S.R. Sutton, M.L. Rivers, K.W. Jones and D.K. Bowen, Adv. X-Ray Anal., 35 (1992) 1265.
14 D. Goossens, L. Van't Dack and R. Gijbels, in D.L. Miles (Ed.), Water–Rock Interaction, Balkema, Rotterdam/Brookfield, 1989, pp. 267–270.
15 K.W. Jones, P. Spanne, G. Schidlovsky, D. Xue, R. Bockman, M. Rabinowits, P. Hammond, R. Bornschein and D. Hoeltzel, in A. Michette, G. Morrison and C. Buckley (Eds.), X-Ray Microscopy III, Springer, Berlin, New York, 1992, p. 431.
16 J.D. Frantz, H.K. Mao, Y. Zhang, Y. Wu, A. Thompson, J. Underwood, R. Giauque, K. Jones and M. Rivers Chem. Geol., 69 (1988) 235.
17 K. Janssens, F. Adams, M.L. Rivers and K.W. Jones, presented at 11th Pfefferkorn Conference, Amherst, MA, August 7–14, 1992.
18 W.T. Elam., Synchrotron Radiat. News, 3 (1990) 14.
19 A. Edwards, D. Sayers., Synchrotron Radiat. News, 3 (1990) 16.
20 A.J. Davenport and H.S. Isaacs, Corros. Sci., 21 (1990) 105.
21 S. Hayakawa, A. Iida, S. Aoki and Y. Goshi, in A. Michette, G. Morrison and C. Buckley (Eds.), X-ray Microscopy III, Springer, Berlin, New York, 1992, p. 376.
22 S. Hayakawa, Y. Goshi, A. Iida, S. Aoki and K. Sato, Rev. Sci. Instrum., 62 (1992) 2545.
23 A. Iida, Trends Anal. Chem., 10 (1991) 215.
24 S.R. Sutton, K.W. Jones, B.M. Gordon, M.L. Rivers, S. Bajt and J.V. Smith, Geochim. Cosmochim. Acta, submitted for publication.
25 G.A. Waychunas, Am. Mineral., 12 (1987) 89.
26 P. Behrens, J. Felsche, S. Vetter and G. Schulz-Ekloff, J. Chem. Soc., Chem. Commun., (1991) 678.
27 M.L. Rivers, S.R. Sutton and K.W. Jones, in A. Michette, G. Momson and C. Buckley (Eds.), X-Ray Microscopy III, Springer, Berlin, New York, 1992, pp. 212–216.
28 M.L. Rivers and S.R. Sutton, National Synchrotron Light Source Annual Report, Brookhaven Natl. Laboratories, Dept. of Energy, Upton, NY, 1990.
29 European Synchrotron Radiation Facility Newsl., No. 14, July (1992), p. 1.
30 L. Vincze, K. Janssens and F. Adams, Spectrochim. Acta, Part B, in press.
31 K. Janssens, L. Vincze, P. Van Espen and F. Adams, X-Ray Spectrom., in press.
32 L. Vincze, K. Janssens and F. Adams, in P.J. Duke, G.W. Lorimer, T. Mulvey (Eds.), Proceedings of the 13th International Conference on X-Ray Optics and Micro Analysis, Manchester, September 1992, in press.
33 S.R. Sutton, M.L. Rivers, S. Bajt and K.W. Jones, presented at the Sixth International PIXE Conference, July 1992.
34 B.A. Carpenter, Adv. X-Ray Anal., 32 (1989) 115.

*Analytica Chimica Acta*, 283 (1993) 111–114
Elsevier Science Publishers B.V., Amsterdam



# Two-photon ionization detection of adsorbed molecules on a metal surface at atmospheric pressure by 355-nm laser irradiation

Hirofumi Kawazumi

*Division of Science, Kitakyushu University, Kokura-minami, Kitakyushu 802 (Japan)*

To-oru Yasuda and Teiichiro Ogawa

*Department of Molecular Science, Kyushu University, Kasuga, Fukuoka 816 (Japan)*

(Received 8th September 1992)

**Abstract**

Two-photon ionization was applied to the sensitive detection of aromatic molecules and dyes on a metal surface in ambient air by using the third harmonic of an Nd:YAG laser. The better quality of the Nd:YAG laser beam compared with a nitrogen laser improved the sensitivity. The detection limits were of the order of $10^{-3}$ monolayer coverage. The dependence of the ionization signal on the molar absorptivity and the metal substrate was measured.

*Keywords:* Surface techniques; Aromatic compounds; Dyes; Laser photoionization; Photoionization spectroscopy

Cleanness is an important characteristic of a surface. For the detection of trace organic molecules on a surface, mass spectrometry using a laser for desorption and ionization is a versatile technique [1–6], although it requires a high-vacuum system. Many practical surface characterization, however, need on-line and in situ measurements under atmospheric pressure.

A laser can be used to ionize a photo-absorbing molecule efficiently through a stepwise multi-photon process. This technique has been successfully applied to the determination of trace amounts of molecules in solution [7–14]. In previous papers [15,16], the highly sensitive two-photon ionization detection of aromatic molecules adsorbed on a metal surface by using a nitrogen laser was reported; photo-current measurement in ambient air is simple and sensitive. Laser radiation of 337 nm provides soft excitation without extensive ionization of the bulk surface, because the photoelectric effect of the metal surface is smaller at 337 nm in comparison with that below 200 nm [17].

In this work, the two-photon ionization detection of aromatic molecules and dyes on metal surfaces under atmospheric pressure by using the third harmonic of an Nd:YAG laser was investigated. The dependence of the ionization signal on the molar absorptivity and the metal substrate was also investigated.

## EXPERIMENTAL

The experimental apparatus and the sample preparation were essentially the same as those reported previously [15,16]. The third harmonic

*Correspondence to:* T. Ogawa, Department of Molecular Science, Kyushu University, Kasuga, Fukuoka 816 (Japan).

0003-2670/93/$06.00 © 1993 – Elsevier Science Publishers B.V. All rights reserved

of an Nd:YAG laser (Quanta-Ray GCR-11, 355 nm, 6 ns) was focused softly on one of the electrodes, on which a sample layer had been prepared. The laser was operated with a pulse energy of 3–4 mJ and a frequency of 3–5 Hz in order to reduce any effects of charging and desorption of the sample. The electrodes were placed in an electrically shielded box. The typical applied voltage was 2.5 kV $cm^{-1}$. The effect of ambient gases was measured in an evacuable chamber with a nitrogen laser (Molectron UV-12, 337 nm, 10 ns).

The photocurrent was measured through a current amplifier (Keithley 427). A time profile was obtained by using a digital storagescope (Iwatsu DS6411) with a time resolution of 10 $\mu$s. A precise signal intensity was obtained by using an A/D converter (Canopus Analog Pro II) with a time resolution of 20 $\mu$s and integrating the signal over 0–200 $\mu$s. The signal intensity was divided by the square of the pulse energy in order to correct for laser fluctuations [14].

A hexane solution (10 $\mu$l) of the sample molecule was dropped into a circular dimple (1.0 $cm^2$) on a metal plate which served as the electrode, then the solution was dried in air. The metal plate was either platinum, copper or nickel. The abbreviations of some of the samples used are 7-amino-4-methylcoumarin = coumarin 440, 1,6-diphenylhexa-1,3,5-triene = DPH, 2,5-bis(5-*tert*-butyl-2-benzoxazolyl)thiophene = BBOT, 2-(4-biphenylyl)-5-phenyl-1,3,4-oxadiazole = PBD and 4,4″-bis[(2-butyloctyl)oxy]-*p*-quaterphenyl = BBQ.

The absorption spectra of adsorbates were recorded on a Shimadzu UV2200 spectrophotometer with a spherical integration attachment.

## RESULTS AND DISCUSSION

The two-photon ionization signal was observed with the laser pulse energy in the range 30 $\mu$J–5 mJ with the metal substrate as the cathode [15,16,18]. The time-resolved photocurrent consisted of a sharp and a broad component; the former was due to fast negative species and the latter from slow negative species. The former was assigned to emitted electrons and the latter to oxygen anions produced by capture of emitted electrons by measuring the dependence of the ambient pressure, applied voltage and ambient gas on the time profile [16].

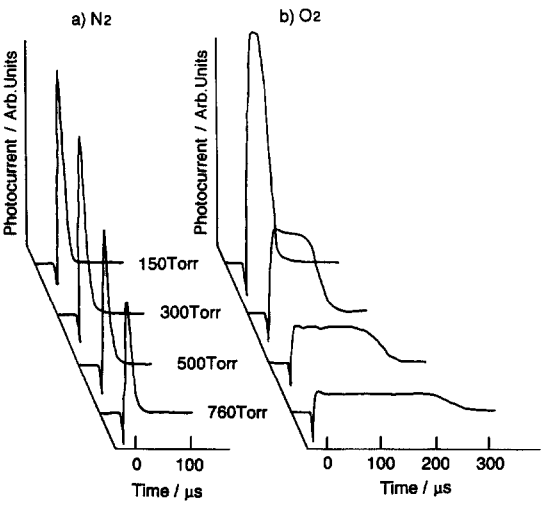


Fig. 1. Time profile of two-photon ionization current from pyrene on platinum in nitrogen and oxygen. Surface density of molecules, $1.0\times10^{-9}$ mol $cm^{-2}$; laser, 250 $\mu$J per pulse at 337 nm; applied voltage, 2.5 kV $cm^{-1}$.

The effects of nitrogen and oxygen as the ambient gas on the time profile are shown in Fig. 1. The sample was pyrene on a platinum plate and the surface density was $1.0 \times 10^{-9}$ mol $cm^{-2}$. The energy of the nitrogen laser was 250 $\mu$J per pulse to avoid space-charge effects. When the chamber is filled with nitrogen, only the sharp component appears. As the time resolution used is slower than the electron drift, a change in the nitrogen pressure induces a corresponding change in the signal intensity but does not affect the time profiles. However, only the slow component appears for oxygen. The time-of-flight behaviour varies with the oxygen pressure because the mobility of the oxygen anion changes steadily. These results confirm the previous assignment of the charge carriers [16].

The signal intensity was proportional to the irradiation area of the laser up to at least 1.5 $cm^2$. The sample was BBQ on a nickel plate and the surface density was $1.0 \times 10^{-10}$ mol $cm^{-2}$. An iris trimmed the laser spot size. The energy of the

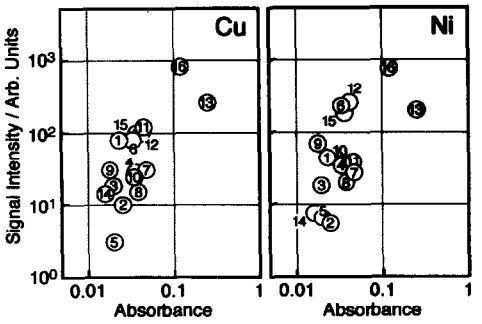


Fig. 2. Dependence of two-photon ionization signal of aromatic hydrocarbons on copper and nickel on absorptivity in ambient air. Surface density of molecules, $1.0 \times 10^{-10}$ mol $cm^{-2}$; laser, 3.0 mJ per pulse at 355 nm. 1 = 9-Methylanthracene; 2 = 1-chloroanthracene; 3 = 9-bromoanthracene; 4 = anthracene; 5 = naphthacene; 6 = 2-methylanthracene; 7 = coumarin 440; 8 = 2-aminoanthracene; 9 = 9,10-dimethylanthracene; 10 = perylene; 11 = DPH; 12 = tetraphene; 13 = BBOT; 14 = PBD; 15 = pyrene; 16 = BBQ.

Nd:YAG laser was 3.5 mJ per pulse at 355 nm when the laser spot size was 1.0 $cm^2$. This finding indicates that the sample molecule adsorbs uniformly on the surface. Two-photon ionization detection with a small laser spot allows a mapping analysis for surface samples by using a beam scanning technique. In subsequent measurements, the whole sample surface was irradiated to increase the sensitivity.

The two-photon ionization signals of sixteen molecules were observed on copper and on nickel and their dependence on the molar absorptivity is summarized in Fig. 2; the absorbance of the adsorbate was measured by using a quartz substrate. The absorption bands of these molecules on the surface shifted to longer wavelengths by more than 10 nm compared with those in hexane solution. The photocurrent of the molecules on copper and nickel is roughly proportional to the absorbance at 355 nm. The effect of the copper and nickel substrate is not as large as that of the molar absorptivity. The efficiency of excitation to the initial singlet excited state seems to be a dominant factor for the ionization. Similar results have been obtained for molecules in solution [9,11,14] and adsorbed molecules excited by a 337-nm nitrogen laser on nickel [17].

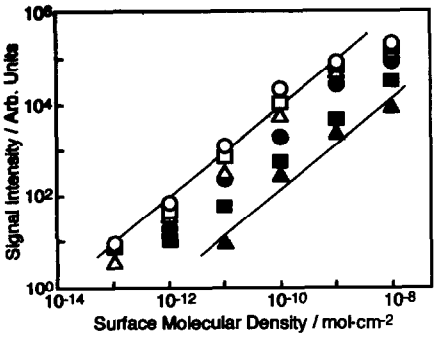


Fig. 3. Analytical response curves of aromatic hydrocarbons on platinum. ○ = BBQ; □ = 2-methylanthracene; △ = pyrene; ● = anthracene; ■ = coumarin 440; ▲ = 1-chloroanthracene. The solid line shows slope = 1.

Analytical response curves were measured for BBQ 2-methylanthracene, pyrene, anthracene, coumarin 440 and 1-chloroanthracene on platinum, as shown in Fig. 3. The surface molecular density was varied by adjusting the concentration of the hexane solution dropped. All the graphs are linear over more than three orders of magnitude. The detection limits of BBQ, 2-methylanthracene, pyrene, anthracene, coumarin 440 and 1-chloroanthracene are $1.0 \times 10^{-13}$, $1.7 \times 10^{-13}$, $2.9 \times 10^{-13}$, $5.5 \times 10^{-13}$, $1.5 \times 10^{-12}$ and $7.1 \times 10^{-12}$ mol $cm^{-2}$, respectively, at signal-to-noise ratio of 3.

The relationship between the detection limits and the molar absorptivities is summarized in Fig. 4. BBQ presents the lowest detection limit ($1.0 \times 10^{-13}$ mol $cm^{-2}$) because of the largest ab-

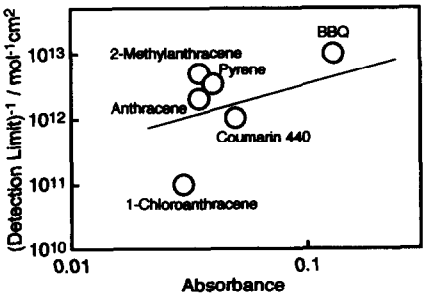


Fig. 4. Detection limits and absorptivities of aromatic hydrocarbons. Absorptivity is evaluated by the absorbance of a $1.0 \times 10^{-10}$ mol $cm^{-2}$ sample on the quartz plate. Solid line shows slope = 1.

sorbance. The detection limit of BBQ corresponds to about 1/500 monolayer coverage, which was estimated by assuming flat adsorption with a surface area of 3 $nm^2$ per molecule. The sensitivity for 1-chloroanthracene is low, probably because initially excited states were quenched by the halogen atom [14]. The detection limits with the Nd:YAG laser are about three times lower than those with a nitrogen laser [15,16], mainly because the former can irradiate a wide area uniformly.

In conclusion, laser two-photon ionization excited by 355-nm laser radiation is a very sensitive technique for trace molecules on a surface in ambient air. As laser radiation with a comparatively long wavelength prevents the photoelectric effect from a bulk metal surface, selective detection of adsorbates has been achieved.

## REFERENCES

1 R. Tembreull and D.M. Lubman, Anal. Chem., 59 (1987) 1003.
2 R.N. Zare, J.H. Hahn and R. Zenobi, Bull. Chem. Soc. Jpn., 61 (1988) 87.
3 B. Stahl, M. Steup, M. Karas and F. Hillenkamp, Anal. Chem., 63 (1991) 1463.
4 S.E. Egorov, V.S. Letokhov and A.N. Shibanov, Chem. Phys., 85 (1984) 349.
5 M. Yang, J.R. Millard and J.P. Reilly, Opt. Commun., 55 (1985) 41.
6 K.R. Gopidas and P.V. Kamat, J. Phys. Chem., 93 (1989) 6428.
7 E. Voigtman, A. Jurgensen and J.D. Winefordner, Anal. Chem., 53 (1981) 1921.
8 S. Yamada, K. Kano and T. Ogawa, Bunseki Kagaku, 31 (1982) E247.
9 S. Yamada, A. Hino, K. Kano and T. Ogawa, Anal. Chem., 55 (1983) 1914.
10 S. Yamada and T. Ogawa, Prog. Anal. Spectrosc., 9 (1986) 429.
11 S. Yamada, T. Ogawa and P.H. Zhang, Anal. Chim. Acta, 183 (1986) 251.
12 N. Sato, S. Yamada and T. Ogawa, Anal. Sci., 3 (1987) 109.
13 S. Yamada, N. Sato, H. Kawazumi and T. Ogawa, Anal. Chem., 59 (1987) 2719.
14 T. Ogawa, M. Kise, T. Yasuda, H. Kawazumi and S. Yamada, Anal. Chem., 64 (1992) 1217.
15 T. Ogawa, T. Yasuda and H. Kawazumi, Anal. Sci., 8 (1992) 81.
16 T. Ogawa, T. Yasuda and H. Kawazumi, Anal. Chem., 64 (1992) 2615.
17 H. Kirihata and M. Uda, Rev. Sci. Instrum., 52 (1981) 68.
18 R. Naaman, A. Petrank and D.M. Lubman, J. Chem. Phys., 79 (1983) 4608.